Available online at www.sciencedirect.com
ScienceDirect
Icarus 191 (2007) 113–131
ICARUS
www.elsevier.com/locate/icarus

East–west trending magnetic anomalies in the Southern Hemisphere of Mars: Modeling analysis and interpretation

Lon L. Hood [a,*], Nicola C. Richmond [a,b], Keith P. Harrison [c], Robert J. Lillis [d]

[a] *Lunar and Planetary Laboratory, University of Arizona, Tucson, AZ 85721, USA*
[b] *Planetary Science Institute, 1700 East Fort Lowell, Suite 106, Tucson, AZ 85719, USA*
[c] *Southwest Research Institute, 1050 Walnut Street, Suite 400, Boulder, CO 80309, USA*
[d] *Space Sciences Laboratory, University of California, Berkeley, CA 94720, USA*

Received 30 November 2006; revised 11 April 2007

Available online 5 May 2007

Abstract

Maps of the vector components of the martian crustal magnetic field over the strongly magnetized Terra Cimmeria/Sirenum region are constructed using Mars Global Surveyor magnetometer data. Although pronounced east–west trending anomalies are present on the radial and north field component maps at the mapping altitude (∼360–380 km), these trends are much less prominent at the lower aerobraking altitude (∼90–150 km). Comparisons with similar maps produced using artificial data at the aerobraking altitude indicate that elongated sources in this region may have maximum lengths along the martian surface of ∼500 km and maximum aspect ratios of ∼2. Iterative forward modeling of several relatively isolated anomalies in the mapped region yields paleomagnetic pole positions consistent with those estimated in previous studies of other anomalies using mapping phase and science phasing orbit data. On this basis, it is inferred that sources in the studied region are most probably magnetized primarily in northward or southward directions. Using this additional constraint, iterative forward modeling is then applied to determine a magnetization distribution that is consistent with data at both the aerobraking altitude and the mapping altitude. The model magnetization distribution, which includes 41 discrete sources, again indicates no highly elongated sources. An examination of surface geology in the region as well as a consideration of the global distribution of anomalies suggests that magmatic intrusions (e.g., subsurface dike swarms), cooling in the presence of water, are the most likely sources of the magnetic anomalies.

Keywords: Mars; Magnetic fields; Mars, interior; Mars, surface

1. Introduction

Maps of the martian crustal magnetic field over the strongly magnetized Terra Cimmeria/Sirenum region centered near the 180° meridian in the Southern Hemisphere show extensive east–west trending features in the radial and north components (Acuña et al., 2001; Connerney et al., 1999, 2001, 2005; Arkani-Hamed, 2002; Cain et al., 2003; Langlais et al., 2004; Hood et al., 2005). These features have previously been attributed to quasi-parallel bands of magnetized crust similar to, but much larger in scale, than those associated with sea floor spreading near terrestrial mid-ocean ridges (Connerney et al., 1999, 2001; Sprenke and Baker, 2000; Whaler and Purucker, 2005). Alternatively, collision and accretion of terranes at convergent plate boundaries has been suggested as a possible explanation for the linear nature of the anomalies (Fairén et al., 2002). Finally, dike intrusions generated either by sea floor spreading or by a moving locus of intrusion sources have also been proposed to explain these anomalies (Nimmo, 2000).

As reviewed by Nimmo and Tanaka (2005), there is no supporting geophysical or geological evidence for the spreading center interpretation of the Terra Cimmeria/Sirenum anomalies. There is also currently little independent (other than magnetic) geophysical or geological evidence for the past occurrence of plate tectonics on Mars. Some analyses of martian crustal magnetic field data have supported the absence of significant plate motions on Mars since the beginning of the core dynamo epoch.

* Corresponding author.
E-mail address: lon@lpl.arizona.edu (L.L. Hood).

0019-1035/$ – see front matter
doi:10.1016/j.icarus.2007.04.025

Specifically, several groups have reported modeling studies of relatively isolated magnetic anomalies to infer bulk directions of magnetization of crustal sources and corresponding paleomagnetic pole positions. Most of these studies have reported pole positions that cluster in an area centered roughly northwest of the Tharsis volcanic complex (Arkani-Hamed, 2001; Hood and Zakharian, 2001; Arkani-Hamed and Boutin, 2004; Hood et al., 2005; Boutin and Arkani-Hamed, 2006). Such a clustering is expected only if Mars was a one-plate planet during and after the core dynamo epoch. This conclusion was first emphasized by Arkani-Hamed (2001) and was later reiterated by Hood et al. (2005). It should be noted that one study (Frawley and Taylor, 2004) reported a modeling analysis that yielded pole positions distributed over a much wider area than that estimated by the former authors. Possible reasons for this difference are discussed in Section 3 below.

In addition to the analysis of individual isolated anomalies, several efforts have been made to construct models of the global martian magnetic field, yielding in some cases models for the vector magnetization distribution in the crust, including that within the Terra Cimmeria/Sirenum region. Both spherical harmonic models (e.g., Arkani-Hamed, 2002; Cain et al., 2003) and equivalent source models (Purucker et al., 2000; Langlais et al., 2004; Whaler and Purucker, 2005) have been produced.

Langlais et al. (2004) modeled magnetic sources as consisting of a mesh of magnetic dipoles located at some assumed depth relative to the mean planetary radius. All three vector components of the MGS magnetometer observations at all altitudes were then used as constraints in a least-squares fit to estimate the amplitude and orientation of each dipole moment vector. Although it was stressed that no unique solution is possible using this technique, the authors experimented with different mesh sizes and depths to evaluate the optimum values of these parameters that yielded the best fit to the available data at both high and low altitudes. The model magnetization distribution was characterized by east–west trending elongations in the radial and northward magnetization components extending over distances as large as 30° of longitude near 50° south latitude.

Whaler and Purucker (2005) modeled martian crustal magnetization using a series of Green's functions relating magnetization at any location in the crust to a given satellite measurement of the crustal field. This had the advantage of producing a spatially continuous crustal magnetization model rather than a model consisting of discrete dipoles. Because an infinity of solutions can satisfy the data equally well, they chose to select the solution that minimized the root-mean-square magnetization intensity in the crust. Their magnetization distribution, like that of Langlais et al., was characterized by east–west trending elongations in the radial and north components extending over 30° in longitude.

In the work of Langlais et al. (2004) and Whaler and Purucker (2005), no a priori constraint on the direction of magnetization in the martian crust was applied. However, as noted above, several modeling studies of relatively isolated martian crustal anomalies have found evidence for clustered paleomagnetic pole positions that, in principle, allow the approximate orientation of the former dynamo dipole moment vector relative to the present-day crust to be inferred. To date, only one study (Arkani-Hamed, 2002) has made use of this directional constraint in order to construct a model of martian crustal magnetization. In his analysis, a degree 50 spherical harmonic model of the martian magnetic potential was inverted to determine the vertically averaged magnetization of a 50 km thick crust. Because of the location of the Terra Cimmeria/Sirenum region near the paleomagnetic equator, the resulting magnetization model in this region was characterized by a weaker radial component and a stronger horizontal component. East–west trends were not present in the model radial magnetization component and were also not prominent in the horizontal component.

In this paper, further mapping and modeling of the magnetic anomalies in the Terra Cimmeria/Sirenum region are reported using an extension of the approach of Hood et al. (2005). One objective of the analysis is to evaluate whether elongated sources are present in the study region. A second objective is to test earlier evidence that the Terra Cimmeria/Sirenum region lies near the paleomagnetic equator inferred from modeling studies of relatively isolated anomalies elsewhere on Mars. A final objective is to apply these results together with available geological and geophysical constraints in order to evaluate further the most probable sources of the observed magnetic anomalies.

2. Data selection, field mapping, and model comparisons

After editing (see below), the data considered here consist of 68 orbits of MGS magnetometer data acquired during the period December 16, 1998 to January 27, 1999 of the MGS aerobraking phase and 355 nightside passes of MGS data acquired during the first 8 months of the mapping phase (March 8–November 16, 1999). These data were initially processed at Goddard Space Flight Center to minimize spacecraft magnetic field interference (Acuña et al., 1999; Connerney et al., 1999) and were obtained from the UCLA Planetary Data System Node. The mapping procedure for the mapping phase data has been described in detail elsewhere Hood et al. (2005). Briefly, external field contributions are first minimized by (a) editing of non-recurring anomalies on adjacent nightside orbit passes; and (b) quadratic detrending over orbit segments with lengths $\gg$ anomaly wavelengths. As in Hood et al. (2005), transient fluctuations at the mapping altitude with amplitudes greater than $\sim$5 nT can be clearly identified as non-crustal in origin. If such fluctuations (defined as deviations from a 10-degree running mean) are present in any one of the three field components, all three components are eliminated during the time period in question. The effective noise level of the resulting maps (used for obtaining model parameter error estimates) is therefore $\sim$5 nT. It is emphasized that the detrending is applied over the entire edited nightside orbit segment (spanning up to approximately 170° of latitude) rather than only the 60° of latitude covered by the maps presented here. This ensures that the orbit segment length is always $\gg$ anomaly wavelengths. The data for each field component and the spacecraft altitude are then filtered two-dimensionally to produce an equally spaced array suitable for contour mapping.

Because of the more variable spacecraft altitude during the aerobraking phase, the mapping procedure applied to the aerobraking data differed somewhat from that applied to the mapping phase data. First, all data (whether obtained on the dayside or nightside) were initially considered and sorted into spatially adjacent passes. Second, only data obtained at altitudes less than 170 km and within the latitude and longitude range of the mapped region (±3°) were accepted. The use of dayside data was judged to be permissible because the accepted data are at relatively low altitudes where anomaly amplitudes (and the ratio of crustal field signal to ionospheric field noise) is relatively high. Because of the large anomaly amplitudes and short lengths of the resulting orbit segments, no quadratic detrending was applied to the aerobraking data. Visual examination of spatially adjacent orbit passes was applied as a final step to eliminate passes containing significant transient field fluctuations while retaining enough passes to produce a contiguous map. At the aerobraking altitude, the threshold for a non-repeating field fluctuation as an indicator of the presence of short-wavelength external fields is ∼50 nT.

Fig. 1 plots the resulting field map at the mapping phase altitude. Plotted are the field magnitude (B-total), the radial, east,

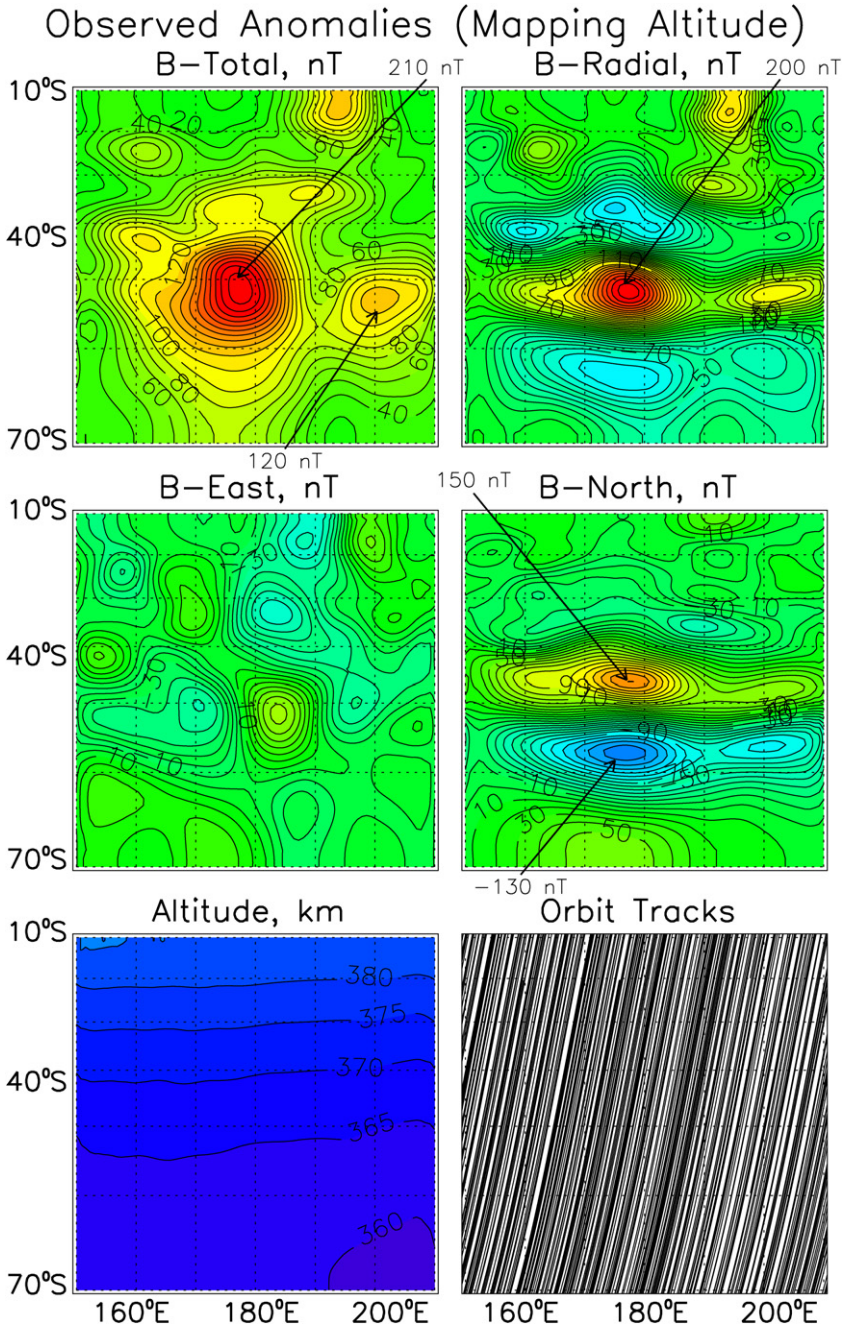

Fig. 1. Contour maps of the magnetic field magnitude and the three vector field components at the mapping altitude over the Terra Cimmeria/Sirenum region. See the text for details of the mapping method. The contour interval on the field plots is 10 nT. The mean MGS altitude and orbit tracks are plotted in the lower two panels.

and north field components, the mean spacecraft altitude, and the surviving orbit tracks on the martian surface. As seen on the orbit track plot, the spatial coverage is essentially complete and all orbit tracks are approximately parallel. As seen on the altitude plot, the mean spacecraft altitude varied smoothly from less than 360 km near the southeast edge of the region to more than 380 km at the northward boundary. A two-dimensional filter size was chosen such that the effective horizontal resolution is 3.75° in longitude and 3.75° in latitude (5 × 5 running boxcar with a bin size of 0.75° in latitude and longitude).

As seen in Fig. 1, the radial and north field component maps exhibit significant east–west trending anomalies in this region as found previously by ourselves and others (references listed in Section 1). The east–west trends are even more pronounced on alternate maps produced at a lower spatial resolution and using different color schemes (see, e.g., Fig. 3 of Hood et al., 2005). The map projection can also introduce east–west stretching of anomalies at the highest latitudes (see, e.g., Hood et al., 2005, and Connerney et al., 2005). Part of the east–west anomaly trends may be attributed to the lower effective resolution in longitude as compared to latitude. However, as shown in Fig. 1, smoothing using a two-dimensional filter with even horizontal resolution does not eliminate the east–west trending anomalies on the radial and north field component maps. Further increases in effective resolution using smaller filter sizes also do not significantly modify the structure of the mapped anomalies. We therefore conclude from Fig. 1 that east–west trends in the radial and north field components are a real characteristic of the crustal anomaly magnetic field at the mapping phase altitude. Furthermore, after careful editing, anomalies in the tangential field components are not significantly more contaminated by induced field noise than those in the radial component, as verified by examinations of stack plots. The absence of east–west trends in the east component and total field are therefore also a real characteristic of the crustal field at this altitude.

Fig. 2 is a map of the vector crustal field at the aerobraking altitude in the same format as Fig. 1 and using the same horizontal resolution of 3.75° in longitude by 3.75° in latitude. As seen in the orbit track plot (lower right of figure), the available spatial coverage at the aerobraking phase altitude is significantly less than at the mapping phase altitude over this region, especially between approximately 160° E and 180° E. For this reason, it is not possible to use a two-dimensional filter size that is smaller than that chosen if a contiguous map is to be produced. The altitude plot (lower left of figure) shows that the effective mean altitude of the map varies from ∼90 to ∼150 km with a mean of about 120 km. Several small regions with little or no useful data are shaded white on this plot. No corresponding white regions are present on the field maps, apparently because the Interactive Data Language contour program interpolates the smaller-amplitude field data. Because of the large mean altitude variations, the mapped crustal field amplitudes differ somewhat from those that would have been obtained if the aerobraking orbit tracks had been at a constant altitude over this region. In principle, it is possible to estimate the fields on a constant altitude surface by least squares fitting an array of vertically oriented dipoles to the field data (e.g., Purucker et al., 2000). However, we have not taken this additional step here since the constructed maps are a valid representation of the data that can be used for visual comparisons with maps constructed from artificial data at the same altitudes as the satellite measurements. The variable mean altitude has no effect on iterative forward modeling (Sections 3 and 4) since the fitting is done by comparing model field component intensities calculated along individual orbit tracks with spacecraft measurements at the same locations.

Comparing the field magnitude plots of Figs. 1 and 2, it is seen that the main large anomaly centered near 52° S, 177° E at the mapping phase altitude is resolved into three quasi-separate anomalies at the aerobraking altitude. The anomaly centered near 57° S, 198° E is more symmetrical and isolated at the aerobraking altitude. A new relatively isolated anomaly near 30° S, 190° E is also mapped at the aerobraking altitude. In general, the anomalies are more fully resolved at the aerobraking altitude even though the horizontal filter size is the same as that applied to the mapping phase data. The field magnitude and east component plots in both figures show little evidence for elongated anomalies. The radial field plot at the aerobraking altitude (Fig. 2) also shows little evidence for east–west trending anomalies. The north component plot at the aerobraking altitude still shows east–west trending anomalies; these anomalies are nevertheless somewhat better resolved than those at the mapping phase altitude. Again, these characteristics cannot be attributed to increased induced field noise in the tangential field components relative to the radial component, as verified by examinations of stack plots of spatially adjacent orbit passes (available from the first author by request).

In order to evaluate initially whether and to what extent elongated sources can be present in the mapped region, maps were constructed similar to Fig. 2 but using artificial data "collected" along the same MGS aerobraking orbit tracks for a variety of possible source geometries and magnetization directions. First, following Hood et al. (2005), thin uniformly magnetized circular sources located at the surface were assumed. At orbital altitudes, this geometry, like the elliptical prism geometry chosen by Arkani-Hamed (2001), is sufficient to represent most source shapes. In particular, source bodies that are elongated or irregularly shaped on scales larger than the spacecraft altitude can be represented by two or more (preferably non-overlapping) adjacent disks whose sizes, locations, and magnetization properties can be estimated by minimizing the RMS deviation between the observed field and the model field. For nearly vertical magnetization directions, forward calculations using single circular sources do not produce elongated anomalies on the field component maps. However, for the case of a nearly horizontal magnetization vector, it was found that the component of the field parallel to the vector produced field component maxima that were somewhat elongated along an axis perpendicular to the vector. To illustrate this characteristic, Fig. 3 shows model field component maps for three separate artificial sources. The anomaly centered at 25° S, 200° E (labeled "A" on the field magnitude plot) is produced by a northwardly magnetized circular source with a radius of 120 km (approximately 2° of latitude). It can be seen that on the radial and north compo-

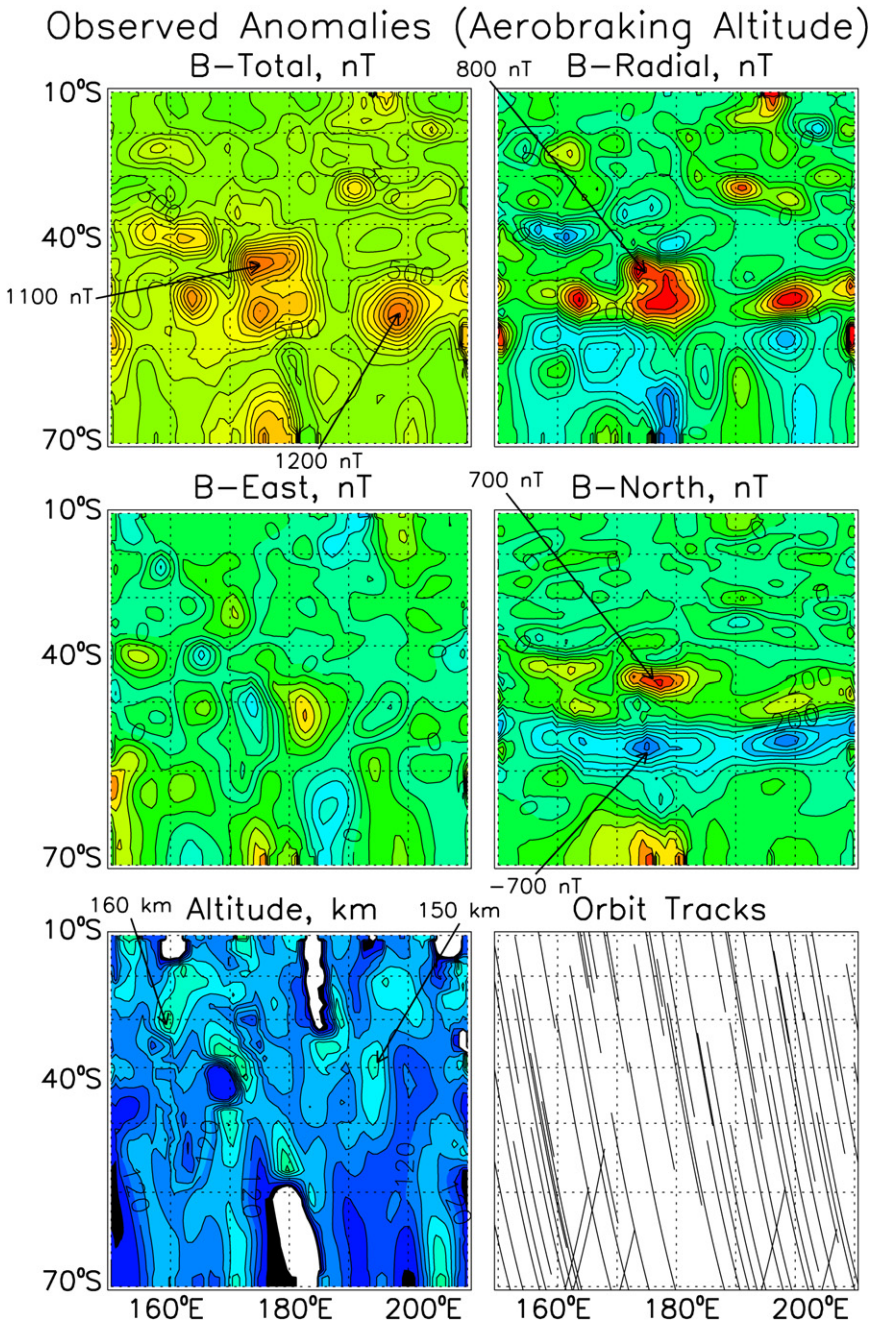

Fig. 2. Same format as Fig. 1 but at the aerobraking altitude using available orbit segments. The contour interval on the field plots is 100 nT. See the text.

nent plots, the contours are elongated in the east–west direction even though the source is circular. Larger east–west elongations of the radial and north component contours are possible if two northwardly or southwardly magnetized circular sources are placed at nearly the same latitude and separated by less than 15° of longitude (not shown here).

To investigate the maximum length and aspect ratio of east–west trending sources within the mapped region, elongated artificial sources were constructed consisting of adjacent circular disks. This geometry was chosen for computational convenience since (a) the software for calculating magnetic fields due to circular disks was already written and available; and (b) general source shapes can be represented by adjacent disks as noted above. Both horizontally and radially inward or outward directions of magnetization were investigated. In Fig. 3, the source of the artificial anomaly centered at 25° S, 160° E (labeled "B") consists of two adjacent 120 km radius circular disks centered at 158° and 162° E, respectively. Both disks are magnetized in a northward direction. The contours on the total field map are now elongated in the east–west direction, unlike the circular anomaly source centered at 200° E. The slight asymmetry of the anomaly is caused by the variable MGS altitude in this region.

Finally, Fig. 3 shows the anomaly components that result from a highly elongated source (labeled "C") consisting of eleven circular disks with radii of 120 km. The disks are cen-

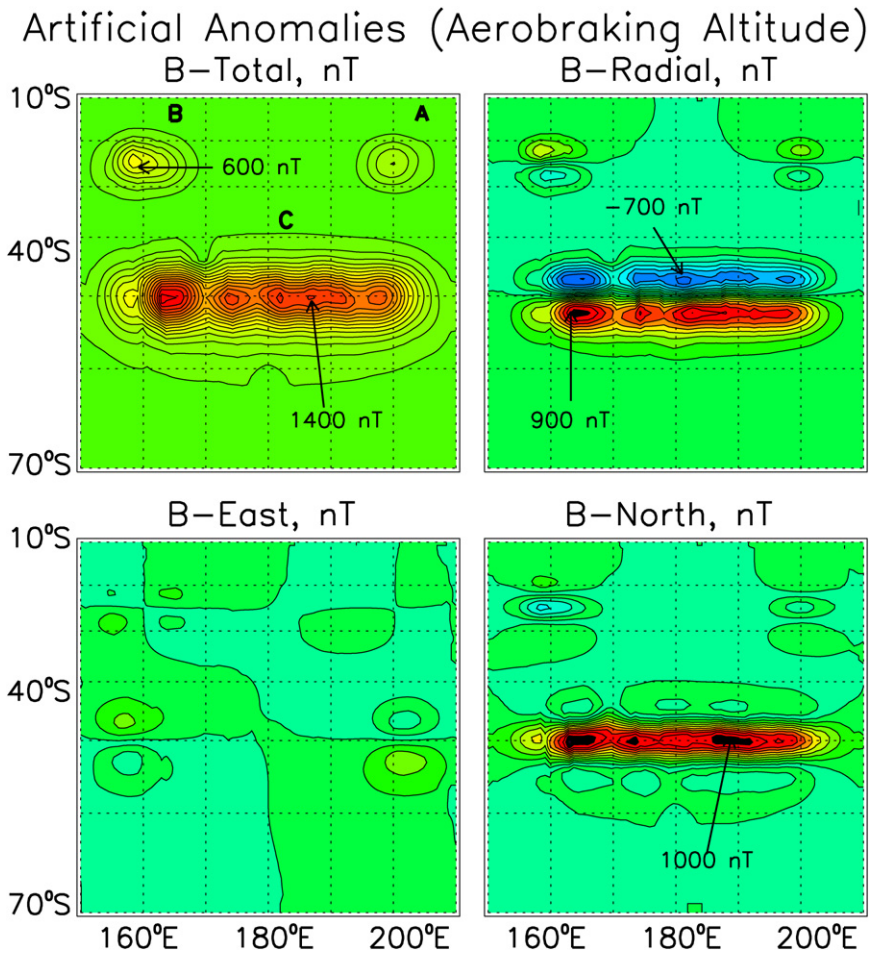

Fig. 3. Contour maps of the magnetic field magnitude and the three vector field components due to the presence of three artificial sources near the martian surface as "collected" along the same aerobraking orbit segments used to produce Fig. 2. The anomalies on the field magnitude plot are labeled "A," "B," and "C." The contour interval on the field plots is 100 nT. See the text.

tered at 50° S and at longitudes ranging from 160° to 200° E at 4° intervals. All disks are magnetized in a southward direction. The radial and northward component plots show pronounced east–west trending anomalies while the east component plot shows only weak anomalies. This is similar to the characteristics of some radial and north field component maps of the actual Terra Cimmeria/Sirenum region. However, unlike the latter maps, the field magnitude plot for this elongated model source also shows a strong east–west trending anomaly.

Based on calculations such as those shown in Fig. 3, one concludes that the field magnitude plot is most diagnostic of the presence or absence of elongated sources. Examination of the actual field magnitude data plot of Fig. 2 (upper left plot) shows that several anomalies have east–west trends comparable to those produced by the two-disk model labeled "B" in Fig. 3. For example, the observed anomaly centered at about 48° S, 175° E is elongated by an amount comparable to that of the two-disk model. However, no observed field magnitude anomalies are elongated significantly more than that of the two-disk model. The absence of total field anomalies with lengths comparable to that of the 11-disk model (labeled "C") in Fig. 3 appears to rule out elongated, uniformly magnetized sources with lengths of thousands of kilometers as was originally suggested by early interpretations of the MGS data over this region. Although no claim is made that these results are unique, we have not yet found an elongated source model that can produce east–west trending anomalies in the radial and north components without simultaneously producing an east–west trending anomaly in the field magnitude. As already stressed above based on stack plots of field component data, it is not possible to attribute the absence of very elongated total field anomalies at the aerobraking altitude to contaminating induced fields in the tangential components. Such stack plots confirm the crustal origin of all significant anomalies plotted in Fig. 2. It is therefore inferred from comparisons such as these that elongated sources with aspect ratios greater than about two and with lengths greater than ∼500 km are unlikely to be present in the Terra Cimmeria/Sirenum region if their magnetization intensities are at least approximately (within a factor of 5 or 10) constant along their lengths.

3. Directional constraints on magnetization models

In order to test the conclusions of the previous section, it is necessary to investigate whether a self-consistent magnetization model for the Terra Cimmeria/Sirenum region can be

constructed that includes only relatively discrete (not highly elongated) sources and yet reproduces the observed east–west trending anomalies. Because the fields in this region are complex and therefore undoubtedly have multiple sources, without further information, it would be extremely difficult to obtain anything approaching a unique solution for the vector magnetization distribution in the crust. Even if only the vertically integrated magnetization distribution is desired, an infinity of solutions can equally well fit the data. To obtain a single solution, one could, following Whaler and Purucker (2005), apply the equivalent source technique under the assumption that the RMS magnetization intensity of the region should be minimized. However, there is no guarantee that this assumption is valid since RMS magnetization intensity increases by a factor of about two or less would be sufficient to yield alternate solutions. Given our current understanding of magnetic carriers and magnetization mechanisms in the martian crust, a factor of two increase in the minimum required mean magnetization intensity (4.76 A/m for a 50 km thick layer; Parker, 2003) cannot be excluded. Alternatively, a knowledge of the direction of magnetization as a function of position in the crust would be sufficient to yield a single solution. For example, one could start with the assumption that all magnetization vectors are radially outward or inward and obtain a good fit to the MGS data for essentially a single source model (see, e.g., Purucker et al., 2000). Unfortunately, the same would be true starting from the assumption that all magnetization vectors are horizontal. Independent constraints on the direction of magnetization as a function of position are therefore needed to obtain a realistic solution.

As reviewed in Section 1, Arkani-Hamed (2002) reduced the non-uniqueness of the problem by assuming that all magnetization vectors in the martian crust are oriented parallel (or anti-parallel) to a dipole field whose moment vector passes through the paleomagnetic pole estimated from modeling of relatively isolated anomalies. His derived magnetization distribution in the Terra Cimmeria/Sirenum region was not highly resolved (because of the 50 degree spherical harmonic model of the global field that was employed) but nevertheless differed substantially from those derived using equivalent source methods under alternate assumptions (Langlais et al., 2004; Whaler and Purucker, 2005).

In general, if a crustal magnetization distribution is complex, consisting of multiple sources with possibly varying directions of magnetization, then it is difficult, if not impossible, to apply orbital magnetometer data to estimate bulk directions of magnetization of anomaly sources. This has been demonstrated, for example, by Ravat (2006) using aeromagnetic survey data for "coalesced" anomalies in a complexly magnetized region of the terrestrial oceanic crust. However, as discussed, for example, by Arkani-Hamed (2002), Hood and Zakharian (2001), and Hood et al. (2005), for the special case in which the magnetization distribution is less complex, consisting mainly of a relatively isolated, approximately uniform magnetization enhancement within a limited crustal volume, then it is possible to apply forward modeling techniques to estimate the bulk direction of magnetization of that source. This is true even if the source actually consists of a group of smaller sources as long as they are all magnetized mainly in one direction. In applying this approach, data selection is important. Only isolated, dominantly dipolar anomalies should be modeled. Even in those cases, some sources of these anomalies may not satisfy the assumptions of the analysis, leading to erroneous directions. The A5 anomaly analyzed by Hood et al. (2005) may fall into this category, for example. Nevertheless, if enough anomalies are analyzed, many or most anomalies can yield approximately valid directions so the approximate paleopole can still be estimated. Using this approach, Arkani-Hamed (2001) analyzed 10 selected anomalies in order to estimate a mean paleomagnetic pole location in the Northern Hemisphere (N.H.) near 25° N, 230° E. Hood and Zakharian (2001) analyzed several northern polar anomalies to estimate a paleopole position in the same general area northwest of Tharsis. From an analysis of seven selected anomalies (many of which were different from those studied by Arkani-Hamed), Hood et al. (2005) estimated the mean paleomagnetic pole location to be 34° ± 10° N, 202° ± 58° E (2σ errors). An alternate analysis by Arkani-Hamed and Boutin (2004) yielded a mean pole position centered near 22° ± 35° N, 232° ± 95° E (see Fig. 6 of Hood et al., 2005). Boutin and Arkani-Hamed (2006) have more recently carried out additional modeling of nine selected anomalies using more detailed data processing and modeling techniques. Their most reliable estimated poles cluster in the same area as those of Arkani-Hamed (2001) and Arkani-Hamed and Boutin (2004).

In principle, one could therefore adopt the method of Arkani-Hamed (2002) and assume that magnetization vectors in the study region are consistent with the mean paleomagnetic pole location estimated by one or more groups. However, we would prefer to have independent information about directions of magnetization in the Terra Cimmeria/Sirenum region that does not depend only on previous paleomagnetic pole estimates. In addition, we would like to test the hypothesis that magnetization directions in the Terra Cimmeria/Sirenum region are consistent with available paleomagnetic pole estimates.

For this purpose, we consider whether any constraints on directions of magnetization can be obtained from the MGS data in the Terra Cimmeria/Sirenum region itself. As noted in Section 2, the map of the region produced from the aerobraking data (Fig. 2) reveals two relatively isolated, high-amplitude anomalies that are potential candidates for iterative forward modeling. These are best identified on the field magnitude map (upper left plot of Fig. 2) as nearly symmetrical maxima that are not adjacent to other strong anomalies. These anomalies are centered at approximately 56° S, 198° E and 33° S, 191° E. Both anomalies can therefore be modeled using the same iterative forward modeling procedure described previously (see Appendix of Hood et al., 2005).

Of these two selected anomalies, the anomaly located at 56° S, 198° E (designated here as A8) is the strongest and is covered by more orbit tracks; it should therefore have the highest ratio of crustal field signal to external field noise. Two opposite-signed radial component maxima are located just north and south of the total field maximum; the east compo-

Table 1
Relatively isolated sources: Magnetization properties (a) and directional properties (b)

(a)

Anomaly	Plate center latitude(s)	Plate center longitude(s)	Plate radii (km)	Dipole moment(s) (A-m^2)
A8	54.5±0.7° S	200.8±0.6° E	110 ± 30	$3.3 \pm 0.5 \times 10^{16}$
	56.2±0.8° S	197.0±0.9° E	100 ± 35	$3.2 \pm 0.6 \times 10^{16}$
A9	33.8±0.9° S	190.4±0.8° E	110 ± 30	$3.1 \pm 0.9 \times 10^{16}$

(b)

	Direction angles		Error cone δ_{95}	N.H. pole position		Error ellipse		
	α	β		λ_{NP}	ϕ_{NP}	Axes		Polarity[a]
						dp	dm	
A8	80 ± 10°	90 ± 10°	10°	38° N	198° E	5°	10°	S
A9	60 ± 15°	65 ± 15°	15°	61° N	248° E	9°	17°	S

[a] N = North magnetic pole (field lines radially outward); S = South magnetic pole (field lines radially inward).

nent is relatively weak and has two oppositely signed maxima centered on the total field maximum; the north component has a strong east–west trending southward maximum centered roughly on the total field maximum. From these characteristics, one expects that the simplest magnetization model would consist of a single northwardly magnetized source. Iterative forward modeling confirms that this is approximately the case. However, the east–west trend of the northward and radial field component anomalies was somewhat stronger than could be simulated using a single circular source. A model consisting of two adjacent circular disks yielded a lower RMS residual. [An equivalent solution could be obtained using an elliptical prism with an aspect ratio of about two (e.g., Arkani-Hamed, 2001).] The addition of more disks with significant magnetic moments would yield higher RMS residuals.

The final model parameters for this anomaly are listed in Table 1 and a comparison of the observed and model field components at the aerobraking altitude is shown in Fig. 4. In particular, the directions of magnetization of the two model disks (assumed to be the same in the modeling) were nearly horizontal and directed northward. Specifically, as listed in Table 1b, the best-fitting direction of magnetization can be described as $\alpha = 80° \pm 12°$, $\beta = 90° \pm 11°$, where α is the angle between the vector and the zenith and β is the azimuth measured counterclockwise from east. In terms of geomagnetic elements, the inclination $I = -10° \pm 12°$ and the declination $D = 0° \pm 11°$. As in Hood et al. (2005), error estimates given in Table 1 are based on maximum deviations of a given parameter needed to increase RMS residuals by an amount comparable to the estimated noise level of the maps (∼50 nT; Section 2). The final RMS residual within an area centered on the anomaly (extending from 62° to 48° S and from 190° to 207° E) was 305 nT. Considering the amplitude of the anomaly (>1300 nT), this is a reasonable agreement.

The second relatively isolated anomaly (∼800 nT) centered near 33° S, 191° E (designated here as A9) is characterized by a single positive radial field maximum and a pair of oppositely signed north component maxima centered on the total field maximum. Its lower amplitude implies a lower signal-to-noise ratio and its reduced coverage implies increased uncertainty in the model fit. Nevertheless, the east component anomaly is again relatively weak and roughly symmetrical about the total field maximum. The southward anomaly on the north component map is somewhat higher in amplitude than the northward anomaly (∼350 vs 250 nT). One therefore expects that the magnetization vector is radially outward and inclined toward the north. Iterative forward modeling generally confirmed this expectation but yielded a best fit for a vector that is inclined somewhat toward the northeast (Table 1b). Specifically, a best fit was obtained for $\alpha = 60° \pm 11°$ and $\beta = 65° \pm 15°$ ($I = -30°$; $D = 25°$). This is apparently due to the fact that the mean spacecraft altitude was somewhat higher to the west of the anomaly maximum than to the east (Fig. 2, lower left plot) so that the mapped westward anomaly was weaker than it would have been if the spacecraft altitude had been constant. As listed in Table 1a, a single circular disk with a radius of 110 km (±30 km) was sufficient to simulate the observed anomaly. The final RMS residual within an area extending from 37° to 28° S and from 187° to 195° E was 216 nT.

From the iterative forward modeling results described above, it is likely that the A8 anomaly source is magnetized in a nearly northward direction. The A9 anomaly (with a lower signal-to-noise ratio and reduced coverage) also probably has a source that is magnetized mostly northward but inclined 30° from the horizontal and 25° toward the east. This somewhat different orientation could be attributed to (a) systematic errors in the modeling (due to the lower signal-to-noise ratio and reduced coverage or to source properties inconsistent with the modeling assumptions); and/or (b) a real difference in the magnetizing field orientation caused by the significant angular separation of the two anomalies and by dynamo secular variations and nondipolar fields. Allowing for reversals of the magnetizing dynamo field, we therefore suggest that the most probable orientation of magnetization vectors in the Terra Cimmeria/Sirenum region is northward or southward. While the possibility of highly variable magnetization directions in this region cannot be excluded, there is no independent evidence that this is the case.

If the martian crust in the Terra Cimmeria/Sirenum region has not undergone large-scale plate motions, we expect that

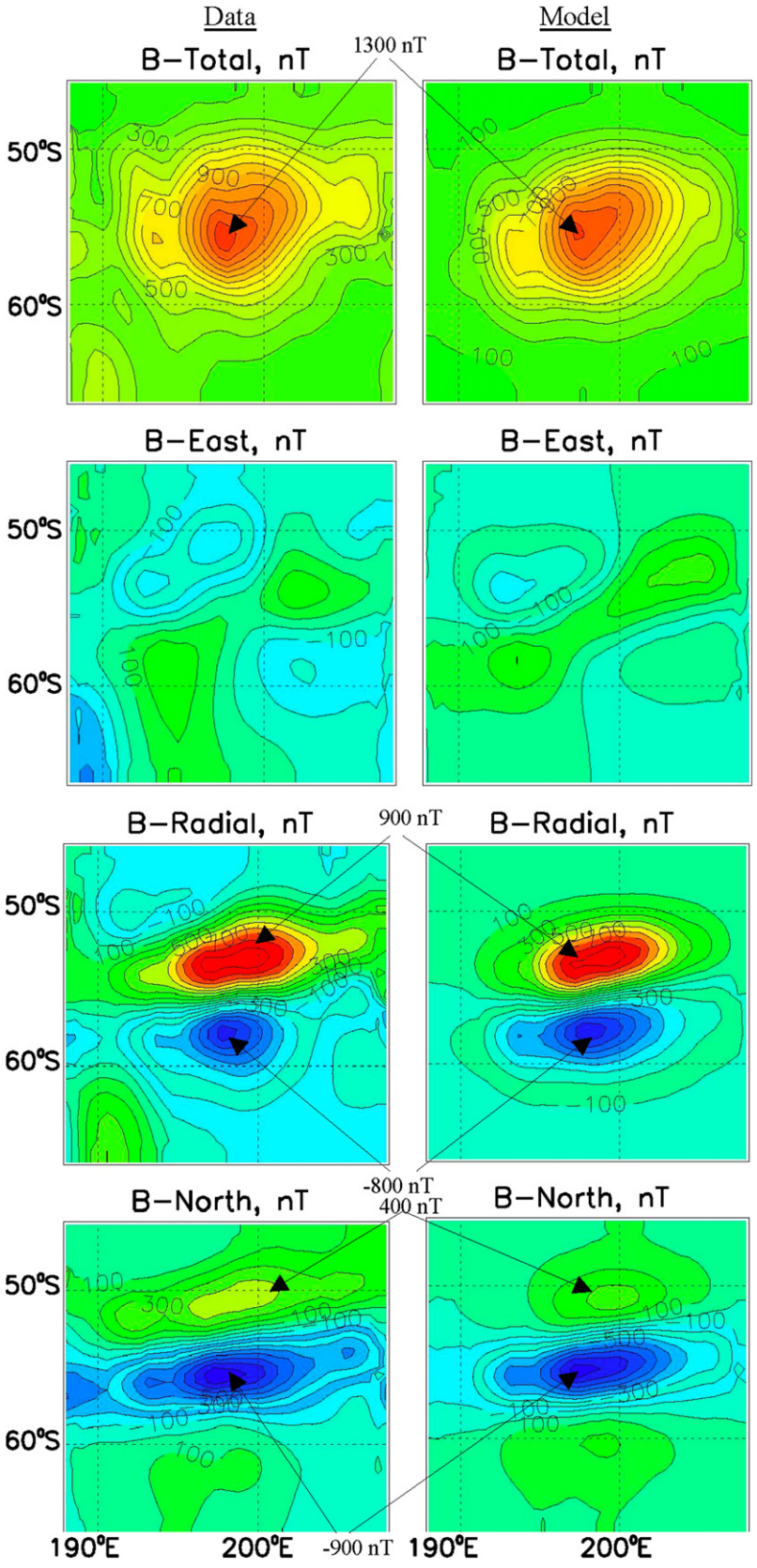

Fig. 4. Comparison of the observed field magnitude and vector field components for the relatively isolated anomaly centered near 57° S, 198° E (designated A8) as calculated from the MGS magnetometer data (left panel) and as calculated from a two-disk source model (right panel) along the same aerobraking orbit segments. The contour interval on the field plots is 100 nT.

the directions of magnetization inferred for the two anomaly sources studied here should yield paleomagnetic pole positions consistent with those estimated in earlier studies. To investigate whether this is the case, we compute corresponding pole positions for the sources of the two modeled anomalies using standard methods (Butler, 1992; Hood and Zakharian, 2001). The resulting south paleomagnetic pole position inferred for the A8 anomaly is calculated to lie at approximately 38° N, 198° E, which is close to the mean pole position estimated by Hood et al. (2005) from an analysis of seven other anomalies. It is also not far from the mean paleomagnetic pole estimated by Arkani-Hamed (2001) and Arkani-Hamed and Boutin (2004). The south paleomagnetic pole position inferred for the A9 anomaly is located at about 61° N, 248° E, which is also in the same area but displaced from the mean pole of Hood et al. (2005) by about 45° of arc. Fig. 5 plots the locations of the pole positions estimated by Hood and Zakharian (2001) (designated A1) and Hood et al. (2005) (designated A2–A7) and the two additional pole positions estimated here (designated A8 and A9). Pole positions in both hemispheres are plotted. It is evident that the two additional positions fall into the same general areas as obtained in previous work. Adding in the two additional positions (and regarding the A5 result as an outlier, as done by Hood et al., 2005), the mean N.H. pole position location with 2σ errors is: 38° ± 20° N, 207° ± 58° E. This mean pole position in each hemisphere is plotted as an open circle with a dot at the center in Fig. 5.

It is of interest to compare the bulk directions of magnetization estimated for the A1–9 sources by Hood and Zakharian (2001), Hood et al. (2005), and in the present work with independent estimates for the same anomalies, where available, reported by Arkani-Hamed and Boutin (2004), Langlais et al. (2004), and Frawley and Taylor (2004). For consistency, all directions will be compared in terms of geomagnetic element angles I (inclination) and D (declination). In the case of the A1 anomaly (65° N, 27° E), the direction estimated by Hood and Zakharian (2001) was $I = 25°$, $D = -10°$ while that estimated by Langlais et al. (2004) was $I = 22°$, $D = -11°$, a very good agreement. No direction estimates for this anomaly were given by the other authors. In the case of the A2 anomaly (12° S, 194° E), the direction estimated by Hood et al. (2005) was $I = -31°$, $D = -10°$ while that estimated by Frawley and Taylor (2004) was $I = -68°$, $D = 170°$, a poor agreement. Again, no estimates are available from the other authors. For the A3 anomaly (35° S, 298° E), the direction estimated by Hood et al. (2005) was $I = -50°$, $D = -56°$; that estimated by Arkani-Hamed and Boutin (2004) (designated anomaly 9 by them) was $I = -41°$, $D = -91°$, a moderate agreement; that estimated by Frawley and Taylor was $I = -15°$, $D = 13°$, a fair agreement. No estimates were provided by Langlais et al. for this anomaly. In the case of the A4 anomaly (6° S, 215° E), the direction estimated by Hood et al. (2005) was $I = -59°$, $D = 137°$; that estimated by Arkani-Hamed and Boutin (2004) (designated as anomaly 4 by them) was $I = -37°$, $D = 146°$, a very good agreement; that estimated by Langlais et al. was $I = -67°$,

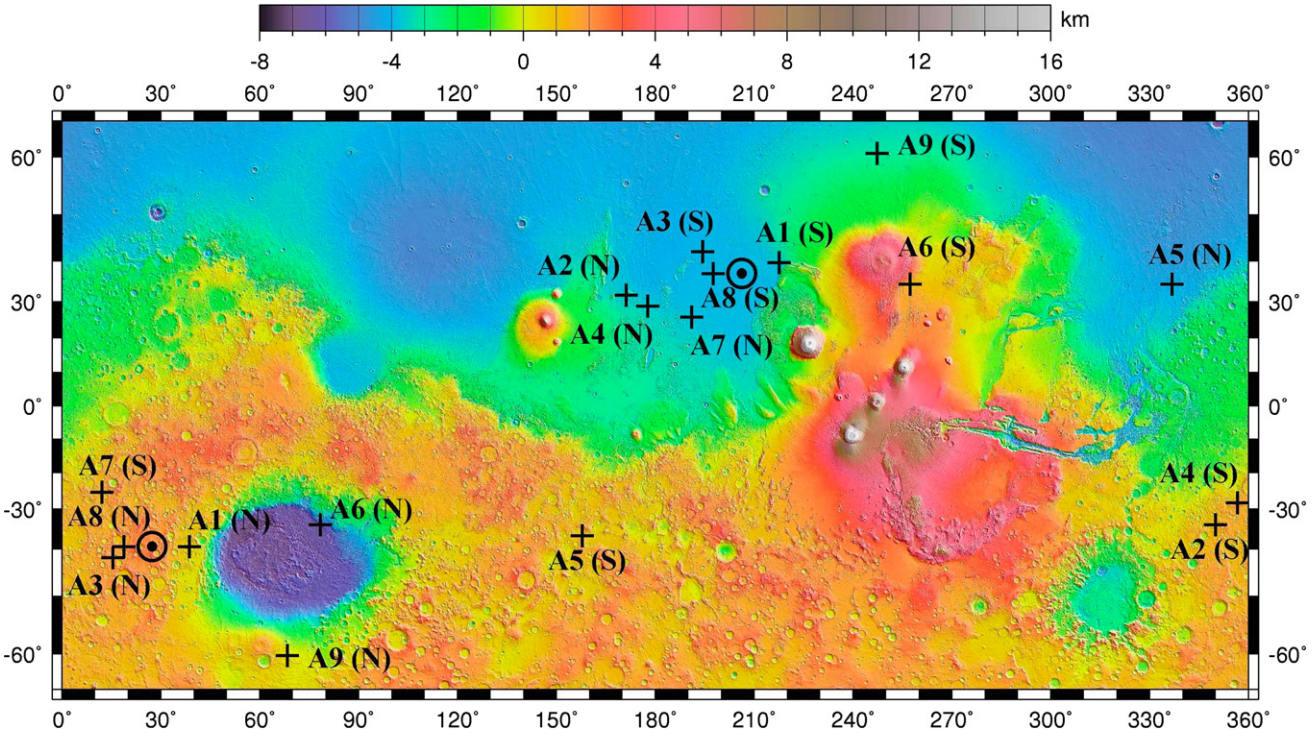

Fig. 5. Paleomagnetic pole locations (superposed on MOLA topography) estimated by Hood and Zakharian (2001) (designated A1), Hood et al. (2005) (designated A2–A7), and the two additional pole positions estimated here (designated A8 and A9). Locations in both hemispheres are plotted and the magnetic polarity of each pole is indicated. The circles with dots in the center indicate the mean paleomagnetic pole location in each hemisphere for all locations except for A5, which is regarded as an outlier.

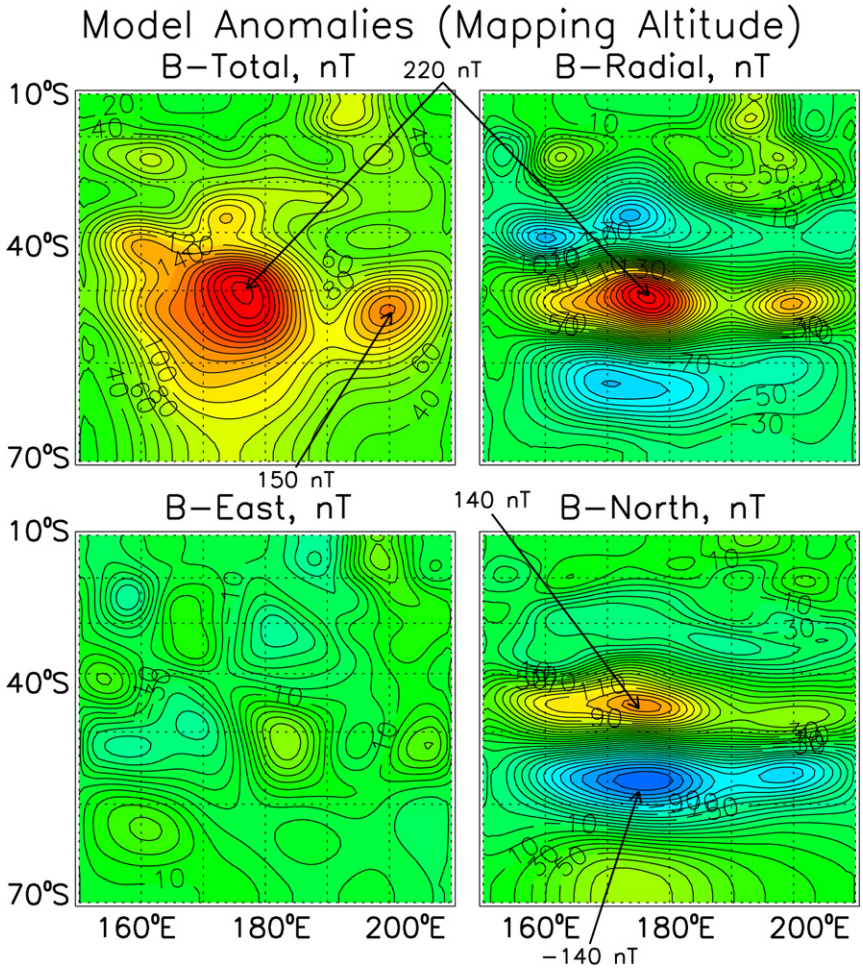

Fig. 6. Final model magnetic field maps at the mapping phase altitude as calculated along the same orbit tracks used to produce the observed field maps of Fig. 1. The source model is listed in Table 2.

$D = -172°$, a fair agreement; that estimated by Frawley and Taylor was $I = -48°$, $D = 4°$, a poor agreement, especially for the declination. In the case of the A5, A6, A8, and A9 anomalies of Hood et al. (2005), no estimates by the other authors are available so no comparisons are possible. In the case of the A7 anomaly (26° S, 254° E), the direction estimated by Hood et al. (2005) was $I = -28°$, $D = 129°$; that estimated by Arkani-Hamed and Boutin (2004) (designated as anomaly 8 by them) was $I = -25°$, $D = 77°$, a moderate agreement; that estimated by Frawley and Taylor for the same anomaly was $I = -30°$, $D = 57°$, a fair agreement. No estimate for this anomaly by Langlais et al. is available.

In general, the mean paleomagnetic pole positions estimated by Hood et al. (2005) and by Arkani-Hamed and Boutin (2004) are in reasonably good agreement (see Fig. 6 of Hood et al., 2005). The more recent study by Boutin and Arkani-Hamed (2006) also yields preferred paleopole estimates that cluster in the same area (see their Fig. 11c). However, the pole positions estimated by Frawley and Taylor (2004) differ substantially from those estimated by the other groups. One contributing factor is that many of the anomalies that they modeled were not relatively isolated and were therefore not well suited for modeling to infer bulk magnetization directions. However, four of the anomalies that they selected were nearly identical to those studied by Hood et al. (2005) (A2, A3, A4, A7) and so should have yielded comparable magnetization directions. In the case of the A2 anomaly, detailed maps of the vector field components were presented by Frawley and Taylor. A direct comparison of these maps to those of Hood et al. (2005) for the same anomaly shows that the mapped north field component differs in important ways from that presented by Hood et al. (2005). In particular, on the Hood et al. (2005) map, the northward anomaly maximum is larger in amplitude than the southward anomaly maximum (65 vs 25 nT). However, on the Frawley and Taylor map, the southward anomaly maximum is larger in amplitude than the northward maximum (35 vs 25 nT). This apparently caused their inferred direction of magnetization, especially the declination, to differ by a large angle from that estimated by Hood et al. (2005). Examinations of data for individual orbit tracks confirm that the northward maximum is indeed larger in amplitude than the southward maximum for this anomaly. It therefore appears that differences in data processing as well as modeling may be responsible for the differences in inferred magnetization directions (and pole positions) obtained by Frawley and Taylor as compared to other groups.

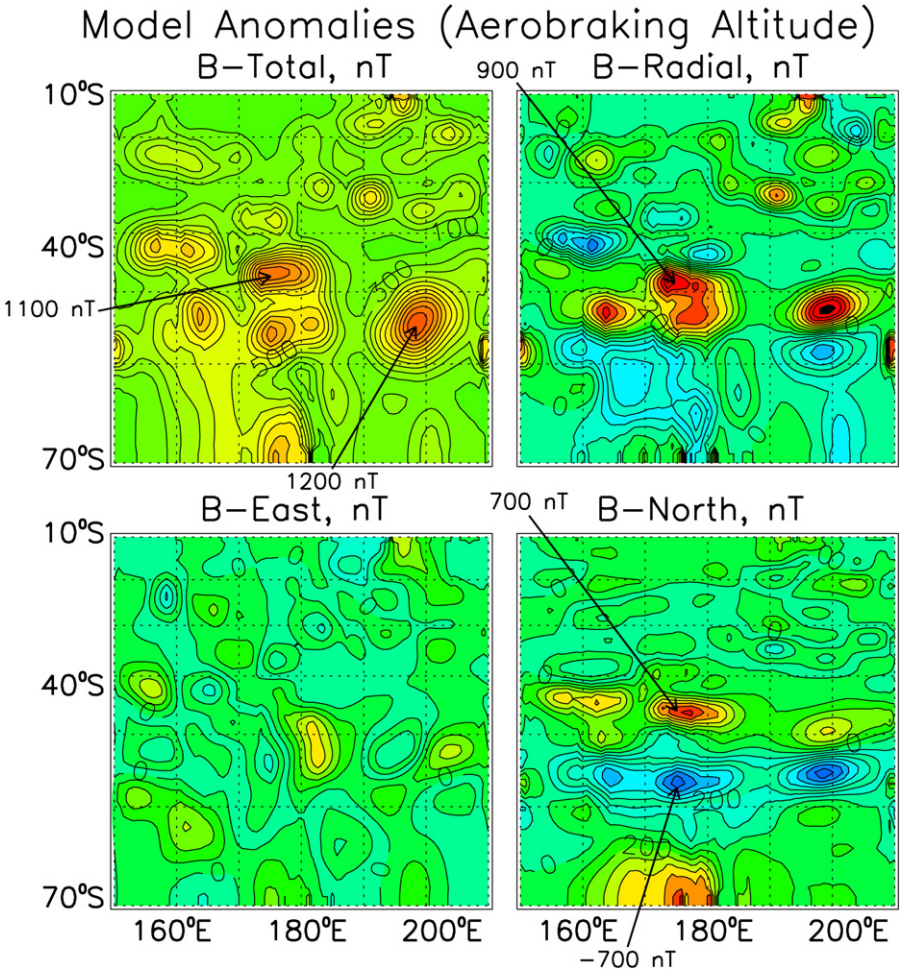

Fig. 7. Same format as Fig. 6 but at the aerobraking altitude as calculated along the same orbit tracks used to produce the observed maps of Fig. 2. The source model is listed in Table 2.

4. Construction of an approximate magnetization model

In order to construct a magnetization model of the studied region consistent with the available MGS magnetometer measurements and with the directional constraint supported by the analysis of the previous section, a modified form of the iterative forward modeling method of Hood et al. (2005) was used. Initially, only the aerobraking data were considered. To make the analysis more manageable, models were first constructed for smaller regions obtained by dividing the 60° × 60° mapped area of Fig. 2 into nine 20° × 20° subregions. In each case, modeling began with one or two circular disk sources (see previous section for justification) located initially beneath total field maxima whose magnetization vectors were initially assumed to be northward or southward. Source parameters (disk sizes, dipole moments, center locations, and directions of magnetization) were then adjusted iteratively as described by Hood et al. (2005) until a minimum RMS deviation was obtained. Additional disks were added where needed until no significant additional reduction of the RMS occurred. Sources from adjacent, previously modeled subregions were included in the model for each successive subregion. All modeled sources were then combined to produce a composite magnetization model of the entire region. A total of 41 disk sources were used in the final composite model. Next, the model magnetic field was calculated along the mapping phase orbits over the same region and a model map at the mapping phase altitude was produced. Although the model map generally agreed with the observed mapping phase map of Fig. 1, the amplitudes of many anomalies differed by small amounts from those on the observed map. It was found that iterative adjustments to the disk radii largely eliminated these differences and reduced the RMS deviation to a minimum at both altitudes. This method takes advantage of the fact that the dependence on altitude of model field amplitudes varies with the radius of a given disk source (the decay with altitude is less rapid for a larger disk radius). Figs. 6 and 7 show the final model magnetic field maps at the mapping phase and aerobraking altitudes, respectively. Within the entire 60° × 60° region, the final RMS deviation of the model field from the observed field along the mapping phase orbit tracks was 34 nT while that along the aerobraking orbit tracks was 259 nT.

Table 2 lists the final model parameters for the 41 disk sources used to simulate the available MGS magnetometer data in the Terra Cimmeria/Sirenum region. Listed are the center coordinates, radii, magnetic moments, magnetic moments per unit area, and local direction angles α and β (defined in Sec-

Table 2
Magnetization model parameters

#	Center lat./long.	Radius (km)	Moment 10^{16} (A-m^2)	Mom./area 10^{16} (A)	Direction angles α	β
1	−24.2°/158.2°	180	4.7	4.6	80°	350°
2	−28.0°/163.2°	90	1.1	4.3	55°	80°
3	−24.8°/168.6°	100	1.6	5.1	80°	80°
4	−20.6°/162.6°	150	1.1	1.6	75°	240°
5	−18.4°/158.2°	180	1.9	1.9	75°	105°
6	−42.8°/156.2°	110	2.9	7.6	110°	245°
7	−44.2°/162.2°	140	3.4	5.5	110°	285°
8	−37.4°/164.8°	160	1.9	2.4	75°	105°
9	−54.6°/164.8°	140	2.3	3.7	55°	65°
10	−56.2°/158.6°	120	2.0	4.4	95°	90°
11	−57.1°/150.0°	100	1.8	5.7	70°	275°
12	−50.7°/162.4°	90	1.5	5.9	75°	240°
13	−62.3°/161.6°	110	1.4	3.7	55°	210°
14	−67.8°/168.0°	170	3.1	3.4	75°	300°
15	−60.2°/166.2°	130	1.0	1.9	120°	90°
16	−19.5°/182.4°	190	2.4	2.1	55°	240°
17	−28.5°/182.0°	190	1.9	1.7	70°	10°
18	−46.3°/173.9°	90	4.4	17.3	75°	265°
19	−46.6°/179.4°	110	3.9	10.3	80°	260°
20	−32.2°/183.8°	90	1.0	3.9	55°	55°
21	−39.6°/174.2°	120	2.5	5.5	105°	275°
22	−38.2°/172.2°	140	1.8	2.9	125°	265°
23	−57.1°/174.5°	110	2.7	7.1	80°	60°
24	−55.6°/179.9°	100	3.9	12.4	75°	95°
25	−69.0°/174.2°	100	1.2	3.8	75°	235°
26	−67.8°/180.8°	80	0.9	4.5	90°	290°
27	−62.6°/184.6°	120	1.2	2.7	135°	35°
28	−62.6°/175.4°	130	1.1	2.1	70°	70°
29	−26.2°/196.2°	160	2.3	2.9	55°	65°
30	−20.1°/202.4°	130	2.7	5.1	110°	240°
31	−20.1°/209.0°	120	1.9	4.2	50°	80°
32	−12.8°/196.0°	110	2.7	7.1	45°	220°
33	−17.9°/190.2°	160	2.8	3.5	40°	60°
34	−33.8°/190.4°	110	3.1	8.2	60°	65°
35	−35.8°/199.0°	90	1.5	5.9	50°	85°
36	−32.6°/206.0°	130	2.3	4.3	85°	95°
37	−46.8°/208.6°	150	2.0	2.8	100°	265°
38	−49.6°/198.0°	140	1.8	2.9	75°	300°
39	−54.5°/200.8°	110	3.3	8.7	80°	90°
40	−56.2°/197.0°	100	3.2	10.2	80°	90°
41	−67.6°/200.2°	80	0.6	3.0	125°	215°

tion 3). It is emphasized that this source model is not unique. Somewhat different source parameters and a slightly smaller RMS could be obtained if more small disks were added to the model in order to simulate more details of the measurements along each orbit track. The present model is only an approximation to the actual vertically integrated magnetization distribution that represents a trade-off between seeking an optimally accurate model and minimizing the amount of necessary labor and computer time. For this reason, no error estimates for individual source parameters are listed in the table. Nevertheless, this source model is sufficient to address the objectives of the analysis regarding the existence of elongated sources and the locations of primary sources. It is representative of the actual vector magnetization distribution if the applied directional constraint is correct.

The magnetization model derived here requires somewhat larger (by factors of 2 to 3) vertically integrated magnetization intensities than have been estimated by previous authors (e.g., Connerney et al., 1999; Whaler and Purucker, 2005). This is at least partly because we have adopted a directional constraint on the magnetization model rather than a minimum magnetization intensity constraint. Specifically, the mean dipole moment per unit area for the sources listed in Table 2 is 5×10^5 A. In order to estimate a corresponding lower bound on the mean magnetization intensity, it is necessary to apply a constraint on the maximum vertical thickness of the crustal source. One bound derived from analyses of martian crustal magnetic spectra is that the maximum source depth is ∼50 km (Voorhies et al., 2002). An alternate constraint is the approximate depth to the Curie isotherm for magnetite whose Curie temperature (580 °C) is relatively high among likely candidate remanence carriers. As reviewed by Hood et al. (2005), during the core dynamo epoch, this depth can be estimated as ∼30 km. For an assumed uniformly magnetized crust with an effective thickness of 30 km, the corresponding mean vertically averaged magnetization intensity for the sources of Table 2 is 17 A/m.

Fig. 8 is a pictorial representation of the distribution of the 41 sources in the Terra Sirenum region superposed on a map of the MOLA topography. Each circle indicates the location of one source disk. The width or boldness of the circle perimeter indicates the dipole moment per unit area of the disk (dipole moment divided by disk area calculated from the parameters listed in Table 2). The arrows indicate the approximate surface projection of the magnetization vector for each source. Note that because the MOLA topography map used here only extends to 65° S, only 37 of the 41 sources are actually shown in the diagram. A scan of the figure shows that most disks are not significantly overlapping and that adjacent disks are usually magnetized in roughly the same direction. One case with significant disk overlap occurs near 40° S, 173° E; however, the estimated magnetization directions are nearly identical so there is no inconsistency with the assumption of a homogeneously magnetized source. Several cases of spatially adjacent disks with differing magnetization directions can be seen (near 20° S, 160° E and 60° S, 165° E). However, the mapped anomalies at these locations are quite weak and so the reliability of the model fit is lower. In any event, the model parameters at these locations do not violate the assumption of homogeneous magnetization within limited crustal volumes since the disks are not significantly overlapping.

An examination of Fig. 8 shows first that there is no apparent correlation of source locations with surface topography including, e.g., large crater locations. Second, although several east–west elongated sources are present, no elongated sources with aspect ratios larger than a factor of 2 or lengths larger than ∼500 km are in the model, which is consistent with the initial analysis of Section 2. However, near a latitude of about 56° S, several northwardly magnetized sources are present that are distributed in longitude between about 160° E and 200° E. Although these consist of discrete sources, their common magnetization in a northward direction would be expected to produce elongated anomalies on the radial and north component maps. Such elongations might be enhanced by the presence of

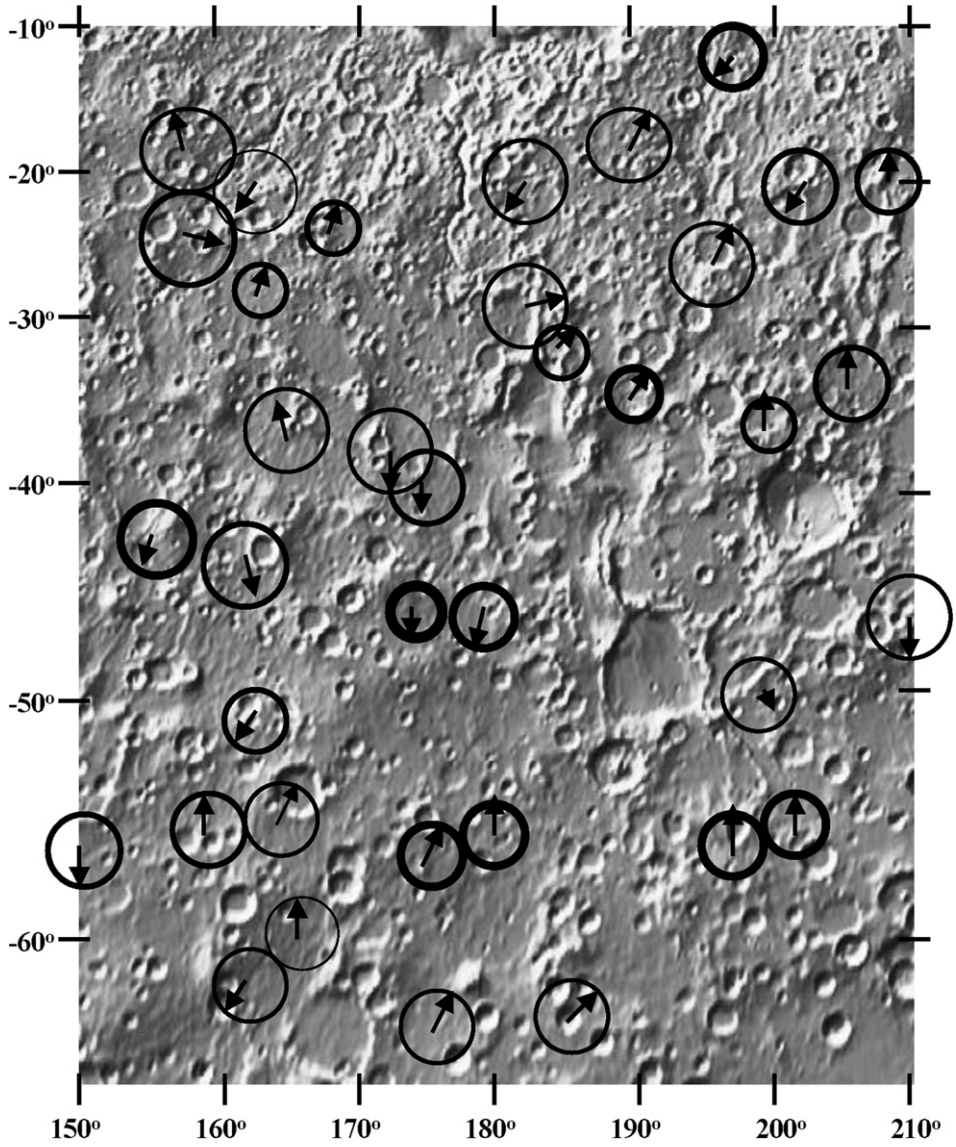

Fig. 8. Approximate locations, sizes, and horizontal components of the magnetization vectors for the sources listed in Table 2 superposed on MOLA topography for the Terra Cimmeria/Sirenum region. The thicknesses of the perimeters indicate qualitatively the amplitude of the dipole moment per unit area of each disk (column 5 of the table).

a strong southwardly magnetized source centered near 46° S, 176° E.

A visual scan of Fig. 8 indicates that the horizontal projections of the model source magnetization vectors tend to be tilted either north-northeast or south-southwest. A calculation of the mean and standard deviations for all β angles less than 180° (i.e., with a partially northward orientation) or greater than 180° (i.e., with a partially southward orientation) confirms this apparent tendency. In the former case, we obtain $\bar{\beta}_N = 75° \pm 22°$ while in the latter case, we obtain $\bar{\beta}_S = 261° \pm 33°$. It is important to note that the vectors were initially assumed to be exactly northward or exactly southward in the iterative forward modeling. Therefore, this tendency is a real indication that the mean orientation of the vectors in the region is close to an axis passing through the northern paleopole, which is located north-northeast of the Terra Cimmeria/Sirenum region (e.g., Fig. 5).

Comparing the model field component maps at the mapping phase altitude (Fig. 6) with the observed field component maps (Fig. 1), the model fields appear to agree reasonably well with the observed fields. In particular, the east–west trends of anomalies on the radial and north field component maps are approximately reproduced. Since the magnetization model consists of discrete sources, the east–west trends on the model maps must be caused by a merging of field components for anomalies originating from separate northwardly or southwardly magnetized sources lying roughly east or west of one another. For example, on the north component plot, the strong east–west trending southward (blue) maximum occurring between about 55° S and 60° S coincides roughly with the locations of a group of northwardly magnetized sources as seen in Fig. 8. Comparing the model field component maps at the aerobraking altitude (Fig. 7) with the observed field maps (Fig. 2), the characteristics of the observed fields again appear to be reproduced reasonably well.

5. Discussion

As discussed in more detail by earlier authors (Hood and Zakharian, 2001; Arkani-Hamed, 2001; Arkani-Hamed and Boutin, 2004; Hood et al., 2005; Boutin and Arkani-Hamed, 2006), assuming that the former martian core dynamo dipole moment vector was roughly aligned with the rotation axis, a location for the northern martian paleomagnetic pole near a latitude of $38° \pm 20°$ requires a major episode of true polar wander between the end of the dynamo epoch and the present. Most planetary dynamo dipole moment axes (i.e., those of the Earth, Mercury, Jupiter, and Saturn) are roughly aligned with their rotation axes and are therefore consistent with the assumption that underlies this conclusion. While it is true that several outer planet dynamo fields (i.e., those of Uranus and Neptune) have dipole moment vectors that are highly inclined to and offset from their rotation axes (60° and 0.3 planetary radii, R_P, for Uranus and 55° and 0.5 R_P for Neptune), the interior structures of these bodies are believed to differ substantially from those of the other planets. Specifically, they probably possess internal ionic water (liquid ice) "oceans" occupying a major fraction of the volumes of their mantles (e.g., Stevenson, 1982). It has been suggested that dynamo action may be occurring in the outer ice layers of both planets and that this is the explanation for the large tilts and offsets of their dipole moment axes relative to their rotation axes (e.g., Stanley and Bloxham, 2004). If so, since the martian dynamo must have been generated in its metallic core, it is more likely that its dynamo behaved more like those of the Earth, Jupiter, Saturn, and Mercury. On this basis, the assumption of a mean alignment of the martian dynamo dipole moment axis with the rotation axis is considered to be reasonable.

Possible independent support for the true polar wander interpretation of the paleomagnetic pole position results of Fig. 5 has been provided by a recent investigation of the rotational stability of Mars prior to the rise of Tharsis (Sprenke et al., 2005). Under some simplifying assumptions, the residual non-hydrostatic martian geoid without Tharsis was estimated and the most stable spin axis was determined. The corresponding N.H. paleopole location was near 30° N, 210° E, i.e., close to that inferred from paleomagnetic anomaly modeling (see Fig. 9a). This close agreement is at least partly fortuitous because of the large error bars on both estimates. However, the fact that the pole position estimated from geoid modeling is in the same general area as that estimated from magnetic anomaly modeling supports both estimates and suggests that the formation of Tharsis was the main cause of the polar reorientation.

As proposed by Hood et al. (2005), the large-scale distribution of crustal magnetic fields on Mars may tend to follow the mean paleomagnetic equator estimated from the anomaly modeling. Fig. 9a compares the mean pole positions (and 2σ deviations) for both hemispheres based on the pole positions plotted in Fig. 5 to a global map of the distribution of crustal magnetic fields. The latter map is produced using the electron reflection (ER) technique (e.g., Lillis et al., 2004; Lillis, 2006) and has an effective altitude of 195 km. The distribution of anomalies shown on this map is similar to that shown on earlier maps derived from low-altitude magnetometer data, e.g., that of Acuña et al. (1999). However, the latter data were not uniformly distributed in altitude on Mars: The aerobraking orbit periapses were mainly in the Southern Hemisphere while the Science Phasing Orbit periapses were mostly northward of 60° N. Therefore, the ER map, which estimates the radial field magnitude near the surface irrespective of the spacecraft altitude, is probably the most accurate available representation of the global field distribution. (Note, however, that the dark east–west bands shown in the Terra Cimmeria/Sirenum region indicate no useful ER measurements caused by an absence of radial fields, which are necessary for electron loss cones to form. They do not indicate east–west bands in the total field magnitude.) As seen in Fig. 9a (as well as the map of Acuña et al., 1999), the distribution of anomalies is controlled to some extent by the location of the dichotomy boundary, which lies at higher northern latitudes near 0° longitude than near 180°. However, it is also clear from Fig. 9a that crustal fields are not homogeneously distributed in the Noachian-aged southern highlands and are not completely absent over some parts of the northern lowlands. For example, fields are weak southwest of Hellas and southeast of Argyre at high paleolatitudes over Noachian-aged highland terrain but are stronger at low paleolatitudes north of Hellas and Argyre extending into portions of the northern lowlands. Taking into account possible modifications to the distribution resulting from later events, the distribution may be best described as a meandering band of anomalies that roughly follows the paleomagnetic equator.

To test this hypothesis quantitatively, one can first assume that the magnetic fields plotted in Fig. 9a are distributed symmetrically about the paleoequator and then determine the most probable location for the corresponding paleopole (Hood et al., 2005). If this location agrees with the paleomagnetic pole, then the hypothesis is supported. For this purpose, we show in Fig. 9b the result of a calculation of the standard deviation (in km) of the latitudinal displacements of high-field ER data bins from the paleoequator corresponding to a given paleopole location. As shown, the minimum standard deviation occurs when the paleopole in the N.H. is located at 46° N, 222° E, which agrees with the paleomagnetic pole plotted in Fig. 9a within the estimated errors. Hood et al. (2005) reported a similar calculation using a global field map constructed from MGS magnetometer data at the mapping altitude yielding an estimated paleopole at 67° N, 201° E. However, the ER map is a more accurate representation of the global distribution of anomalies because of its lower effective altitude and, hence, greater sensitivity to weaker fields over the N.H. Future work is needed to confirm this apparent agreement and, in particular, test the extent to which the curvature of the dichotomy boundary may bias the results shown in Fig. 9b.

According to the analysis of Section 4, as summarized in Table 2 and shown schematically in Fig. 8, the present results indicate that the sources of anomalies in the Terra Cimmeria/Sirenum region have a fairly random distribution and are not elongated by more than ~500 km in any direction. These results therefore do not support interpretations involving either spreading centers or accretion of terranes at con-

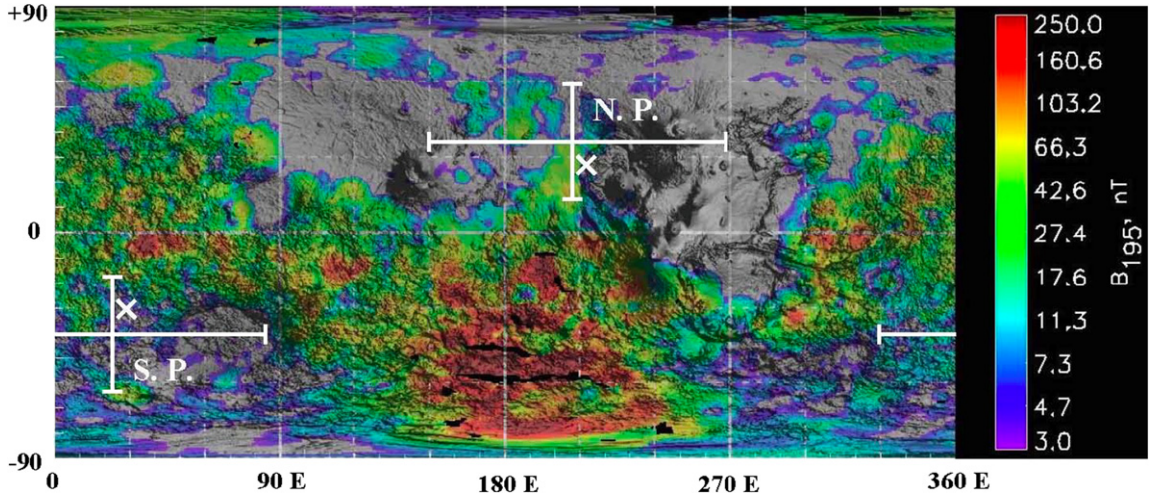

(a)

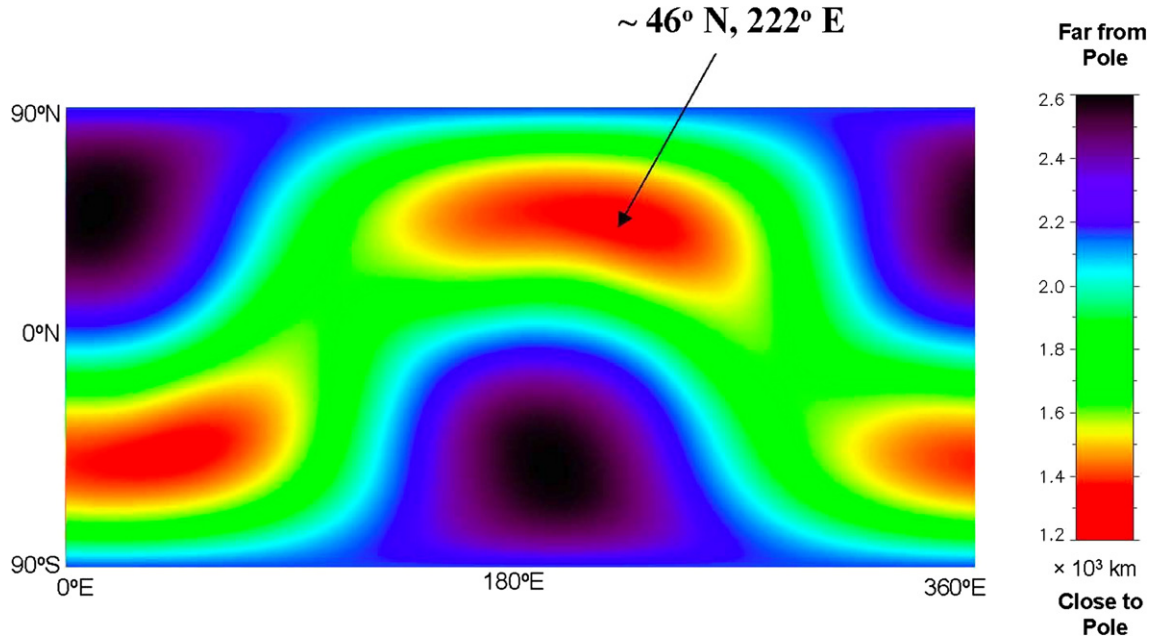

(b)

Fig. 9. (a) Global distribution of martian crustal magnetic fields at an effective altitude of ~195 km as mapped using the electron reflection technique (Lillis, 2006). Also indicated are the locations of the northern and southern paleomagnetic poles as estimated from the data of Fig. 5 (white error bars) and the location of the martian paleopole prior to the formation and growth of Tharsis as estimated by Sprenke et al. (2005) (white 'x'). (b) Standard deviation (km) of the latitudinal displacements of high-field bins (i.e., bins for which the field magnitude is greater than the mean value of 31.8 nT) from the paleoequator corresponding to a given assumed paleopole location. Red indicates locations near the most probable paleopole, which is identified in the Northern Hemisphere by the arrow.

verging plate boundaries. Geologic units in the study region include Noachian aged cratered plateau material and, to a lesser extent, Noachian aged hilly and cratered material (Scott and Carr, 1978). The cratered plateau material is characterized by flat and smooth intercrater terrain and partially buried craters, interpreted as being caused by volcanic lava flows and aeolian resurfacing. The hilly and cratered material is characterized by rugged intercrater terrain, interpreted to imply relatively little volcanic and aeolian resurfacing. A number of grabens and faults are present in the region with a tendency for an east-northeast/west-southwest orientation (De Hon, 1977; Batson et al., 1979). Most of these grabens are probably underlain by sheet-like dike intrusions (Mège and Masson, 1996). However, many radiate from Tharsis and most or all probably post-date the dynamo epoch. There is no clear association between the observed grabens and the inferred anomaly source locations plotted in Fig. 8. Nevertheless, dike swarms beneath pre-existing grabens overlain by the plateau volcanic lava flows and aeolian deposits could be the anomaly sources.

It has previously been suggested that dike intrusions are the sources of the anomalies (Nimmo, 2000). This suggestion was motivated, in part, by the need for narrow, sheet-like intrusions (<2 km wide) in order to provide cooling rates sufficiently rapid to produce magnetically stable single-domain magnetite grains (assumed to be the main magnetic carrier). One criticism of this model is that faults interpretable as grabens are

pervasively present on the surface of Mars (e.g., McKenzie and Nimmo, 1999). One would therefore expect magnetic anomalies of comparable intensity to be present all across the Noachian-aged southern highlands. As a further constraint on the origin of the anomaly sources, it is useful to consider the global distribution of martian crustal fields. Specifically, as discussed above, this distribution appears to be characterized by a concentration toward the location of the paleomagnetic equator, which passes nearly through the Terra Cimmeria/Sirenum region. One hypothesis for explaining this distribution is that (a) hydrothermal processes were involved in producing the strong anomalies; and (b) near-surface water was more abundant at low latitudes where surface ice or water may have been more stable during most of the core dynamo epoch (in contrast to the present era). Crystallization of a basaltic magma in the presence of water can significantly increase the formation rate of magnetite (Weitz and Rutherford, 1999). The presence of water can also increase the cooling rate of a magmatic intrusion with consequences for magnetization acquisition. This possibility is supported by the observed tendency for the valley networks (dendritic channels produced mainly by ground water flow; e.g., Carr and Head, 2003) to occur mainly at low latitudes and to have a large-scale distribution similar to that of the crustal magnetic fields (Jakosky and Phillips, 2001; Harrison and Grimm, 2002; Hood et al., 2005). Therefore, a variant of the Nimmo (2000) model in which dike intrusions form in the presence of upper crustal water may be suggested.

Finally, it is clear that the Terra Cimmeria/Sirenum anomalies have unusually high amplitudes compared to others on Mars. It is therefore necessary to consider why this is the case. Several possible explanations have been offered. Solomon et al. (2005) suggest that anomalies elsewhere in the southern highlands have reduced amplitudes because of long-term hydrothermal demagnetization of pre-existing anomaly sources due to enhanced presence of water in the lowest-lying parts of drainage basins. Also, Kletetschka et al. (2004) suggest that magnetic sources in the Terra Cimmeria/Sirenum region are more strongly magnetized than elsewhere because the remanence carriers there have an unusually high coercivity. Finally, it was originally suggested that anomalies in this region are relatively strong because this is the only area in the southern highlands that escaped substantial shock demagnetization from basin-forming impacts and thermal demagnetization associated with Tharsis volcanism (Hood et al., 2003). The latter authors considered only demagnetization by the primary impact shock waves produced by the Hellas, Argyre, and Isidis impacts. It was suggested that this demagnetization could have extended out to several basin radii, thereby affecting magnetization intensities in a large part of the southern highlands. However, Mohit and Arkani-Hamed (2004) later pointed out that, because the primary impact shock wave decays rapidly with decreasing depth, if martian magnetic sources are at relatively shallow depths in the crust (<50 km), the primary impact shock wave would produce little demagnetization. They therefore argued that demagnetization should not have extended beyond the basin rim.

Artemieva et al. (2005) have more recently shown that if magnetic sources in the martian crust are at relatively shallow depths, then most shock demagnetization would have been caused by secondary ejecta impacts. Demagnetization by secondary impact shock waves is effective at shallow depths out to a number of basin radii for large basins such as Hellas and Argyre. Therefore, secondary impact demagnetization may allow the impact shock mechanism for explaining the amplitude of the Terra Cimmeria/Sirenum anomalies to be realized after all. Kletetschka et al. (2004) have argued that shock demagnetization associated with the small (∼800 km diameter) Prometheus basin (located near the present south pole) would have reduced the magnitude of these strong anomalies if the remanence carriers in the region had coercivities comparable to those found elsewhere on Mars. However, as shown by Artemieva et al. (2005), the efficiency of secondary shock demagnetization at shallow depths is a strong function of basin size. Basins less than 1000 km in diameter, such as Prometheus, will be much less effective in demagnetizing the near-surface layer at a given number of basin radii. This could explain why the Terra Cimmeria/Sirenum region was relatively unaffected by the adjacent Prometheus impact without a difference in coercivity (and composition) of remanence carriers in this region.

6. Conclusions

In this paper, improved maps of the vector components of the martian crustal magnetic field at both the MGS mapping altitude and at aerobraking altitudes have been constructed over the strongly magnetized Terra Cimmeria/Sirenum region. On the basis of these maps and other analyses reported above, the following main conclusions may be drawn:

(1) Strong east–west trends in the north and radial field components are present at the mapping altitude. However, at the lower aerobraking altitude, these trends are no longer present on the radial component map and are much less pronounced on the north component map. Examinations of spatially adjacent orbit plots (stack plots) demonstrate that the mapped tangential components as well as the radial component are not greatly contaminated by induced field noise. The reduced east–west trends at lower altitudes therefore represent a real property of the martian crustal magnetic field.
(2) Iterative forward modeling of two relatively isolated anomalies at the aerobraking altitude yield estimated directions of magnetization that tend to be horizontal and tilted toward the north. The corresponding paleomagnetic pole positions fall within an area consistent with several previous analyses of other such anomalies around Mars, implying that the Terra Cimmeria/Sirenum region was located near the paleomagnetic equator.
(3) Assuming initially that bulk magnetization vectors in the region are mainly oriented in northward or southward directions (based on (2) above), an approximate magnetization model of the region can be constructed that is consistent with available data at both the mapping and aerobrak-

ing altitudes. The resulting model, together with forward calculations for a variety of source parameters, indicate the absence of elongated near-surface sources with lengths greater than ∼500 km.

(4) The east–west trending anomalies present on some north and radial field component maps of the region are most probably caused by a merger of these field components, especially at the higher mapping altitude, due to discrete sources being magnetized mainly in northward or southward directions and lying roughly to the east or west of one another.

(5) A comparison of a recent MGS ER map of the global distribution of crustal magnetic fields with the mean paleopole location inferred from modeling of 9 relatively isolated martian anomalies supports previous suggestions that the crustal field distribution tends to follow the mean paleomagnetic equator. However, future work should consider the extent to which the curvature of the dichotomy boundary may artificially influence these results.

(6) There is no clear correlation of the inferred locations of magnetic anomaly sources in the region with surface geology or topography. However, a consideration of likely martian remanence carriers (e.g., magnetite) together with geologic evidence suggests that subsurface magmatic intrusions were involved in the formation of anomaly sources. A reasonable working model is that of Nimmo (2000) in which swarms of relatively thin dike intrusions are the sources.

In addition to these main conclusions, it was speculated in Section 5 that the presence of upper crustal water may have enhanced the production of magnetite in the dike intrusions and/or increased the cooling rates so that both single-domain magnetite production and acquisition of TRM in the dynamo field were more efficient (see also Rochette, 2006). Water ice may have been stable mainly at low latitudes during the core dynamo epoch as is known to be true for obliquities >40° (Mischna et al., 2003). Alternatively, if the climate was episodically warmer than it is today, liquid water, rather than ice, may have been stable at low latitudes during low obliquities. Evidence of paleolakes in craters and other depressions suggest that liquid water was stable under some conditions, although ice covers may have been present. This would help to explain the concentration of anomalies near the paleoequator as well as the broad spatial correlation of valley networks with crustal fields. Finally, it was suggested that magnetic anomalies in the Terra Cimmeria/Sirenum region may be stronger than those elsewhere on Mars because only this region escaped shock demagnetization associated with secondary impacts from major basin formation and thermal demagnetization associated with Tharsis volcanism and the resurfacing of the northern lowlands.

Acknowledgments

Support for this work under Grant NNG06GA16G from the NASA Mars Data Analysis Program is appreciated. Useful criticisms of an earlier manuscript by two anonymous reviewers are also appreciated. The version of the MOLA topography data used in this paper was provided by D. Smith and the MOLA team. The acquisition of the MGS magnetometer data from the UCLA Planetary Data System node was assisted by S. Joy. Planetary Science Institute publication #411.

References

Acuña, M., Connerney, J., Ness, N.F., Lin, R., Mitchell, D., Carlson, C., McFadden, J., Anderson, K., Rème, H., Mazelle, C., Vignes, D., Wasilewski, P., Cloutier, P., 1999. Global distribution of crustal magnetization discovered by the Mars Global Surveyor MAG/ER experiment. Science 284, 790–793.

Acuña, M., Connerney, J.E.P., Wasilewski, P., Lin, R., Mitchell, D., Anderson, K., Carlson, C., McFadden, J., Rème, H., Mazelle, C., Vignes, D., Bauer, S., Cloutier, P., Ness, N.F., 2001. The magnetic field of Mars: Summary of results from the aerobraking and mapping orbits. J. Geophys. Res. 106, 23403–23417.

Arkani-Hamed, J., 2001. Paleomagnetic pole positions and pole reversals of Mars. Geophys. Res. Lett. 28, 3409–3412.

Arkani-Hamed, J., 2002. Magnetization of the martian crust. J. Geophys. Res. 107 (E5), doi:10.1029/2001JE001496. 5032.

Arkani-Hamed, J., Boutin, D., 2004. Paleomagnetic poles of Mars: Revisited. J. Geophys. Res. 109, doi:10.1029/2003JE002229. E03011.

Artemieva, N., Hood, L.L., Ivanov, B.A., 2005. Impact demagnetization of the martian crust: Primaries versus secondaries. Geophys. Res. Lett. 32, doi:10.1029/2005GL024385. L22204.

Batson, R.M., Bridges, P.M., Inge, J.L., 1979. Atlas of Mars. NASA Scientific and Technical Information Branch, Washington, DC. 146 pp.

Boutin, D., Arkani-Hamed, J., 2006. Pole wandering of Mars: Evidence from paleomagnetic poles. Icarus 181, 13–25.

Butler, R.F., 1992. Paleomagnetism: Magnetic Domains to Geologic Terranes. Blackwell Sci., Malden, MA, 319 pp.

Cain, J.C., Ferguson, B., Mozzoni, D., 2003. An $n = 90$ internal potential function of the martian crustal magnetic field. J. Geophys. Res. 108 (E2), doi:10.1029/2000JE001487.

Carr, M.H., Head, J.W., 2003. Basal melting of snow on early Mars: A possible origin of some valley networks. J. Geophys. Res. 30 (24), doi:10.1029/2003GL018575. 2245.

Connerney, J.E.P., Acuña, M., Wasilewski, P., Ness, N., Rème, H., Mazelle, C., Vignes, D., Lin, R., Mitchell, D., Cloutier, P., 1999. Magnetic lineations in the ancient crust of Mars. Science 284, 794–798.

Connerney, J.E.P., Acuña, M.H., Wasilewski, P.J., Kletetschka, G., Ness, N.F., Rème, H., Lin, R.P., Mitchell, D.L., 2001. The global magnetic field of Mars and implications for crustal evolution. Geophys. Res. Lett. 28, 4015–4018.

Connerney, J.E.P., Acuña, M.H., Ness, N.F., Kletetschka, G., Mitchell, D.L., Lin, R.P., Reme, H., 2005. Tectonic implications of Mars crustal magnetism. Proc. Natl. Acad. Sci. 102, 14970–14975.

De Hon, R., 1977. Geologic Map of the Eridania Quadrangle of Mars. US Geol. Surv. Misc. Inv. Ser. Map I-1088.

Fairén, A.G., Ruiz, J., Anguita, F., 2002. An origin for the linear magnetic anomalies on Mars through accretion of terranes: Implications for dynamo timing. Icarus 160, 220–223.

Frawley, J.J., Taylor, P.T., 2004. Paleopole positions from martian magnetic anomaly data. Icarus 172, 316–327.

Harrison, K.P., Grimm, R.E., 2002. Controls on martian hydrothermal systems: Application to valley network and magnetic anomaly formation. J. Geophys. Res. 107 (E5), doi:10.1029/2001JE001616.

Hood, L.L., Zakharian, A., 2001. Mapping and modeling of magnetic anomalies in the northern polar region of Mars. J. Geophys. Res. 106 (E7), 14601–14619.

Hood, L.L., Richmond, N.C., Pierazzo, E., Rochette, P., 2003. Distribution of crustal magnetic fields on Mars: Shock effects of basin-forming impacts. J. Geophys. Res. 30 (6), doi:10.1029/2002GL016657. 1281.

Hood, L.L., Young, C.Y., Richmond, N.C., Harrison, K.P., 2005. Modeling of major martian magnetic anomalies: Further evidence for polar reorientations during the Noachian. Icarus 177, 144–173.

Jakosky, B.M., Phillips, R.J., 2001. Mars' volatile and climate history. Nature 412, 237–244.

Kletetschka, G., Connerney, J.E.P., Ness, N.F., Acuña, M.H., 2004. Pressure effects on martian crustal magnetization near large impact basins. Meteorit. Planet. Sci. 39, 1839–1848.

Langlais, B., Purucker, M., Mandea, M., 2004. Crustal magnetic field of Mars. J. Geophys. Res. 109, doi:10.1029/2003JE002048. E02008.

Lillis, R.J., 2006. Electron Reflectometry as a Probe of the Martian Crust and Atmosphere. Ph.D. Dissertation, Univ. of California, Dept. of Physics, Berkeley, CA, 253 pp.

Lillis, R.J., Mitchell, D.L., Lin, R.P., Connerney, J.E.P., Acuña, M.H., 2004. Mapping crustal magnetic fields at Mars using electron reflectometry. Geophys. Res. Lett. 31, doi:10.1029/2004GL020189. L15702.

McKenzie, D., Nimmo, F., 1999. The generation of martian floods by the melting of ground ice above dykes. Nature 397, 231–233.

Mège, D., Masson, P., 1996. A plume tectonics model for the Tharsis province, Mars. Planet. Space Sci. 44, 1499–1546.

Mischna, M.A., Richardson, M.I., Wilson, R.J., McCleese, D.J., 2003. On the orbital forcing of martian water and CO_2 cycles: A general circulation model study with simplified volatile schemes. J. Geophys. Res. 109 (E6), doi:10.1029/2003JE002051. 5062.

Mohit, P.S., Arkani-Hamed, J., 2004. Impact demagnetization of the martian crust. Icarus 168, 305–317.

Nimmo, F., 2000. Dike intrusion as a possible cause of linear martian magnetic anomalies. Geology 28, 391–394.

Nimmo, F., Tanaka, K., 2005. Early crustal evolution of Mars. Annu. Rev. Earth Planet. Sci. 33, 133–161.

Parker, R.L., 2003. Ideal bodies for Mars magnetics. J. Geophys. Res. 108 (E1), doi:10.1029/2001JE001760. 5006.

Purucker, M., Ravat, D., Frey, H., Voorhies, C., Sabaka, T., Acuña, M., 2000. An altitude-normalized magnetic map of Mars and its interpretation. Geophys. Res. Lett. 27, 2449–2452.

Ravat, D., 2006. Uncertainty in magnetization directions derived from planetary magnetic anomalies in view of numerical experiments with coalesced anomalies from Earth. Eos Trans. AGU (Fall Suppl.) 87 (52). Abstract GP11B-0076.

Rochette, P., 2006. Crustal magnetization of Mars controlled by lithology or cooling rate in a reversing dynamo? Geophys. Res. Lett. 33, doi:10.1029/2005GL024280. L02202.

Scott, D.H., Carr, M.H., 1978. Geologic Map of Mars. US Geol. Survey Misc. Geol. Inv. Map I-1083.

Solomon, S.C., Aharonson, O., Aurnou, J., Banerdt, W.B., Carr, M., Dombard, A., Frey, H., Golombek, M., Hauck II, S., Head III, J., Jakosky, B., Johnson, C., McGovern, P., Neumann, G., Phillips, R., Smith, D., Zuber, M., 2005. New perspectives on ancient Mars. Science 307, 1214–1220.

Sprenke, K.F., Baker, L.L., 2000. Magnetization, paleomagnetic poles, and polar wander on Mars. Icarus 147, 26–34.

Sprenke, K.F., Baker, L.L., Williams, A.F., 2005. Polar wander on Mars: Evidence in the geoid. Icarus 174, 486–489.

Stanley, S., Bloxham, J., 2004. Convective-region geometry as the cause of Uranus' and Neptune's unusual magnetic fields. Nature 428, 151–153.

Stevenson, D.J., 1982. Interiors of the giant planets. Annu. Rev. Earth Planet. Sci. 10, 257–295.

Voorhies, C.V., Sabaka, T.J., Purucker, M., 2002. On magnetic spectra of Earth and Mars. J. Geophys. Res. 107 (E6), doi:10.1029/2001JE001534. 5034.

Weitz, C.M., Rutherford, M.J., 1999. Petrological explanations for the magnetic anomalies detected on Mars. In: Fifth Int. Conf. on Mars, Lunar and Planetary Institute Contribution 972. Lunar and Planetary Institute, Houston, TX. Abstract 6162 (CD-ROM).

Whaler, K., Purucker, M., 2005. A spatially continuous magnetization model for Mars. J. Geophys. Res. 110, doi:10.1029/2004JE002393. E09001.